Advances in Science and Technology Research Journal, 2026, 20(1), 74–88 https://doi.org/10.12913/22998624/209069 ISSN 2299-8624, License CC-BY 4.0

An improved algorithm for polarisation plane rotation angle measurement

Grzegorz Kozieł¹©

¹ Faculty of Electrical Engineering and Computer Science, Lublin University of Technology, Nadbystrzycka 38A, 20-618 Lublin, Poland E-mail: g.koziel@pollub.pl

ABSTRACT

Sensors using tilted fibre Bragg gratings (TFBG) are now widely used and intensively developed due to their high precision, interference immunity, small size and low price. One of the parameters that can be measured with them is the angle of light polarisation plane rotation (LPPR) propagating in the optical fibre. Existing TFBG sensors are based on measuring the power of light at a selected wavelength, which results in a limited measurement range and low precision. Other methods are based on advanced algorithms that process a selected range of the TFBG spectrum using a wavelet (DWT) or fast Fourier transform (FFT). However, achieving high precision over the entire measurement range is impossible due to the similar FFT and DWT coefficient variation. In the present study, it was identified that a cascaded connection of two TFBGs, rotated relative to each other, allows for obtaining the variability function of the cladding mode minima (MMC₁) shifted in relation to one another as a function of the LPPR angle. This enables direct utilisation of the minima values in the algorithm calculating the LPRR angle based on the light spectrum. Furthermore, the obtained MMC, functions exhibit a significantly lower level of interference than the previously employed FFT coefficient variability waveforms. These phenomena were used to develop a method for calculating the measurement result from the measured light spectra. Based on the cladding mode minima values measured for angles 0°, 2°, 4°,..., 180°, a calibration was conducted. An algorithm was developed to select the MMC, functions that will be used to calculate the measured rotation angle. The developed solution allows measuring the light polarisation plane rotation angle with equal precision in the range of 0-180°. Applying the proposed method has improved the measurement's stability. Compared to existing solutions, MAE was improved by 2.6% and MSE by 66%.

Keywords: TFBG, Bragg, polarisation, fibre, sensor, interference, optic, measurement.

INTRODUCTION

Modern measurement systems increasingly employ light as a means of conveying information. This trend is evident in both telecommunications and in industry. The low attenuation of optical fibres and their low sensitivity to electromagnetic interference are essential here [1]. The creation of Bragg structures in the core of an optical fibre allows for producing highly sensitive sensors that can measure various physical quantities [2, 3]. Proper utilisation of optical fibre sensors allows for monitoring the parameters of various devices and materials [4, 5].

However, attention must be paid to the type of fibre used [6, 7]. Tilted Bragg gratings (TFBG) have special properties. Because they reflect part of the light towards the fibre cladding, they allow sensitivity to environmental parameters to be achieved [8, 9]. Apodisation of Bragg gratings enables the reduction of side lobes and the filtering of the required frequencies [10]. Additionally, optical fibres are often coated with substances. That changes their refractive index when in contact with certain substances [11, 12]. In this way, it is possible to create chemical and biological sensors [13, 14]. The issue with TFBG sensors is their sensitivity to polarisation

Received: 2025.07.07

Accepted: 2025.09.06

Published: 2025.11.21

rotation [15]. Some works attempt to reduce the polarisation influence but this technology is not perfect yet [16].

Without external influences, TFBGs can be used to study the parameters of light propagating through an optical fibre. One such application is the measurement of the angle of rotation of the polarisation plane of light propagating through an optical fibre [17, 18]. The methods used to date to measure the angle of rotation of the polarisation plane of light propagating through an optical fibre use a single TFBG. In the case of hardware-based methods based on analysing the power of light transmitted at a specific wavelength, the measurement range is significantly limited, and the precision is low [17, 18]. In the case of spectrum analysis methods, reduced measurement precision is observed in specific rotation angle ranges and complex calculations are required to obtain the result [19, 20].

However, it is worth noting that all parameters of the light spectrum propagating through TFBG that can be used to measure the angle of rotation of the light polarisation plane vary periodically with changes in the polarisation plane angle [19, 20]. These functions have a flattened response near the extremes. These extremes occur when the plane of polarisation of light aligns with or is perpendicular to the normal to the axis of symmetry of the TFBG. Consequently, using two TFBGs rotated relative to each other by a certain angle should produce shifted but related functions.

It is also worth noting that the changes in the spectrum caused by the change in the angle of LPPR occur in the cladding modes region [19]. In the case of TFBGs with different parameters, these regions may occur at different wavelengths. This makes it possible to connect TFBGs in series and record their spectra using a single optical spectrum analyser (OSA). If these TFBGs are rotated relative to each other by a certain angle, then with appropriate analysis of the spectrum of light propagating through such a TFBG cascade, it will be possible to record the response of both TFBGs and obtain a sensor that allows stable and precise measurement of the angle of LPPR in the range of 0–180°.

The main goal of the paper is to develop an interrogation system and method for measuring the angle of LPPR using a cascade of two TFB-Gs. This will enable reliable measurement of the LPPR angle with consistent precision throughout the entire measurement range.

The rest of the paper is organised as follows: the related works section provides background on the literature. The materials and methods section includes a description of the measurement system, the proposed method for calculating the LPPR angle, and the transformations and measures used. The results and their analysis are presented in the results and discussion section. The entire text is summarised in the conclusions section.

RELATED WORKS

The measurement of the LPPR angle using TFBG is performed indirectly. The measurement system's response is the intensity of light propagating at a specific wavelength or the light spectrum propagating through TFBG. The results obtained need to be converted into the angle of LPPR. Light spectra are treated as continuous or discrete signals. Popular transformations used in signal analysis are used to convert them into a measurement result [21, 22]. These are primarily the wavelet and Fourier transforms. The appropriate selection of features used to calculate the result is also important [23]. Incorrect selection or selection of a noisy part of the signal has a negative impact on the measurement result.

Methods based on measuring the intensity of light propagating at a selected wavelength were proposed in [17, 18]. In [17] an OSA was used to record the spectrum of light propagating through TFBG. The transmission coefficient for different LPPR angles at a chosen wavelength was read from the spectrum obtained. The wavelength was selected to ensure the transmission coefficient was measured at the wavwlength where the minimum of the selected mode S occurs. At the minima of the modes, there is a significant change in the transmission coefficient in response to a change in the LPPR angle. In [18], a hardware solution was used. A FBG was used to reflect a narrow range of light wavelengths covering the entire width of the S mode of the TFBG transmission spectrum. The power of the reflected light was then measured using an optical power meter. In both cases, the results obtained were similar. An almost linear relationship was obtained between the measured light power and the LPPR angle in the range of 25–70°. A flattening of the tested characteristics was observed in the vicinity of rotation angles of 0°, 90° and 180°. It was impossible to distinguish between the ranges of 0-90°

and 90–180°. The authors also did not examine the accuracy offered by the proposed methods. Due to the way the research was conducted, the above reports should be treated as demonstrating the possibility of using the analysed relationships to perform the mentioned measurements, rather than as ready-made methods.

Methods for measuring the angle of LPPR based on advanced processing of the light spectrum propagating through TFBG are presented in [19, 20]. They use the Fourier transform[19] and the wavelet transform [20] to process a selected fragment of the light spectrum. The obtained transform coefficients are subjected to complex numerical processing in order to obtain their variability curves as a function of the angle of LPPR. Both methods allow the LPPR angle to be measured in the range of $90^{\circ} - 180^{\circ}$. Despite using different transforms and different methods of transforming the obtained coefficients, the same problem was encountered in both cases. The variability curves are flattened out for LPPR angles that are multiples of 45°. This results in reduced measurement precision in the vicinity of these angles.

Another interesting phenomenon is the potential to use variations in the position of a selected cladding mode minimum to ascertain the LPPR angle. It has been shown that the minima of the cladding modes adjust their positions with changes in the LPPR angle [24]. However, no method has been proposed to measure the LPPR angle.

MATERIALS AND METHODS

Tilted fibre Bragg gratings

TFBG is a periodic perturbation in the refractive index generated in the core of an optical fibre. It should be understood as a group of parallel planes characterised by a refractive index different from that of the rest of the fibre core. Various methods exist for producing Bragg structures [25, 26]. For this work, the structures were produced by exposing the fibre to UV light using a phase mask method [27, 28]. Since the mask was positioned at a certain angle Θ to the fibre axis, the planes created are tilted relative to the normal of the fibre axis at the same angle Θ , resulting in the formation of tilted Bragg structures – TFBG.

The light reaching the TFBG is partially reflected. Some of the light that is reflected along

the fibre core is known as Bragg resonance. Another portion is reflected by the Bragg structures towards the fibre cladding, creating cladding modes in the transmission spectrum, which consists of a series of minima whose size depends on the TFBG parameters and the angle of incidence of polarised light on the Bragg structures. A diagram of the TFBG with the propagation of light inside the Bragg structures is shown in Figure 1.

For the purposes of this work, two TFBGs were created: one with Θ =6° and the other with Θ =10°. The transmission spectra of the produced TFBGs are illustrated in Figure 2.

The selection of the tilt angles of the TFB-Gs was intentional, not random. A TFBG with a small angle Θ reacts weakly to changes in polarisation [17]. The cladding modes of TFBGs with similar tilt angles occur at similar wavelengths. When TFBGs are connected in series, they overlap, making it difficult or impossible to read the measurement results. Another limitation is the wavelength range in which the available laboratory light source emits light. Therefore, TFBGs were selected such that their cladding mode areas overlap only slightly, which does not affect the effectiveness of the measurements, while also occurring within the wavelength range where the source emits significant light power. This approach enabled the acquisition of signals with substantial power and a high signal-to-noise ratio.

Interrogation setup

The measuring system comprises a superluminescent diode (SLED) that transmits light through an optical fibre to a collimator, creating a parallel beam that propagates in air. This beam passes through a polariser and an electronically

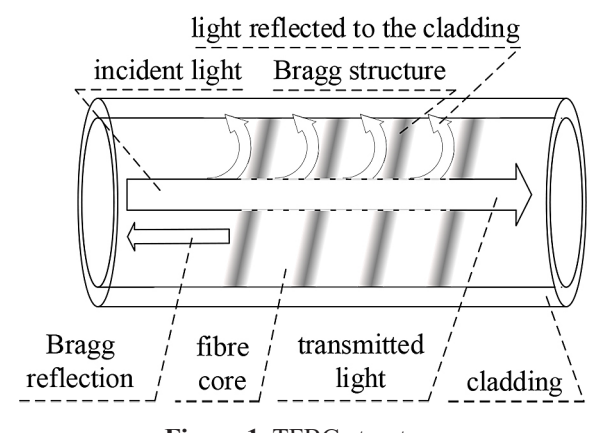
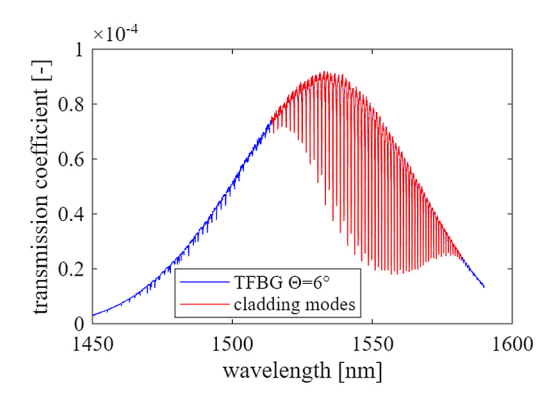


Figure 1. TFBG structure



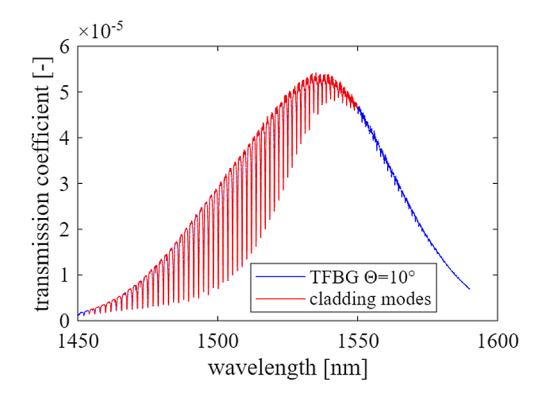


Figure 2. Used TFBGs spectra

rotated half-wave plate, allowing for changes to the LPPR angle. The light is then directed through a second collimator to an optical fibre, where two TFBGs are placed in series. Each TFBG is mounted in manipulators that secure them and enable rotation to any angle. The spectrum of light propagating through the TFBGs is recorded by the OSA. A diagram of the measurement system is shown in Figure 3.

Before beginning the measurements, the collimators were positioned with 3D tables to maximise the light power reaching the TFBGs. Additionally, the polariser was adjusted to the setting that produced the highest light power propagating through the system. Subsequently, both TFBGs were aligned using manipulators to achieve P polarisation. After this, TFBG 2 was rotated by an angle of 23 degrees. The system, prepared in this way, was maintained for an hour to stabilise the operating temperature of all components.

Measurements

The measurements were preceded by setting the half-wave plate in its initial position through a so-called homing operation. This position corresponds to a rotation angle of 0°. The spectrum of light propagating through the system was recorded, after which the plane of polarisation of the light was rotated by a specified angle, and the spectrum was recorded again. This procedure was repeated until a rotation of 180° was achieved. An example of the spectrum of light propagating through the system is shown in Figure 4. Each spectrum was measured in the 1450–1590 nm range with a resolution of 0.004 nm, resulting in a series of 35,001 values (samples).

For this study, measurements were taken with a resolution of 1 degree, while calibration

measurements were conducted with a resolution of 2 degrees. This resolution was selected to evaluate measurement errors across the range of rotation angles for which the system was calibrated. Using a higher resolution for calibration allows for more precise detection of changes caused by variations in the angle of rotation but requires a greater number of measurements. The choice of the measurement and calibration resolution was also influenced by the fact that the same resolution was used in [19, 20]. This enabled a reliable comparison of the obtained results.

Feature extraction

The measured light spectra contain features that are useful for determining the LPPR angle. The power of light propagating at wavelengths corresponding to the minima of the cladding modes is collected from the complete recorded light spectrum. Since the minima slightly change their position, the first step is to identify the wavelength of light for which the spectrum values will be recorded. For this purpose, spectra measured for LPPR angles $\alpha = \{0^{\circ}, 23^{\circ}, 90^{\circ}, 113^{\circ}\}$ were selected. This selection of angles is justified by the fact that the S and P modes reach their lowest values for LPPR angles of 0° and 90°, respectively. Since TFBG 2 is rotated by 23° relative to TFBG 1, using angles 23° and 113° enabled the smallest minimum values from TFBG 2 to be obtained. Next, the locations of the minima were identified, and the wavelengths at which these minima occur were taken as the wavelengths where they reach their lowest values. The observation dictated this choice that at these wavelengths, the changes in light power reach their highest values. The spectra of the selected cladding modes with their assigned rotation angles are presented in Figure 5.

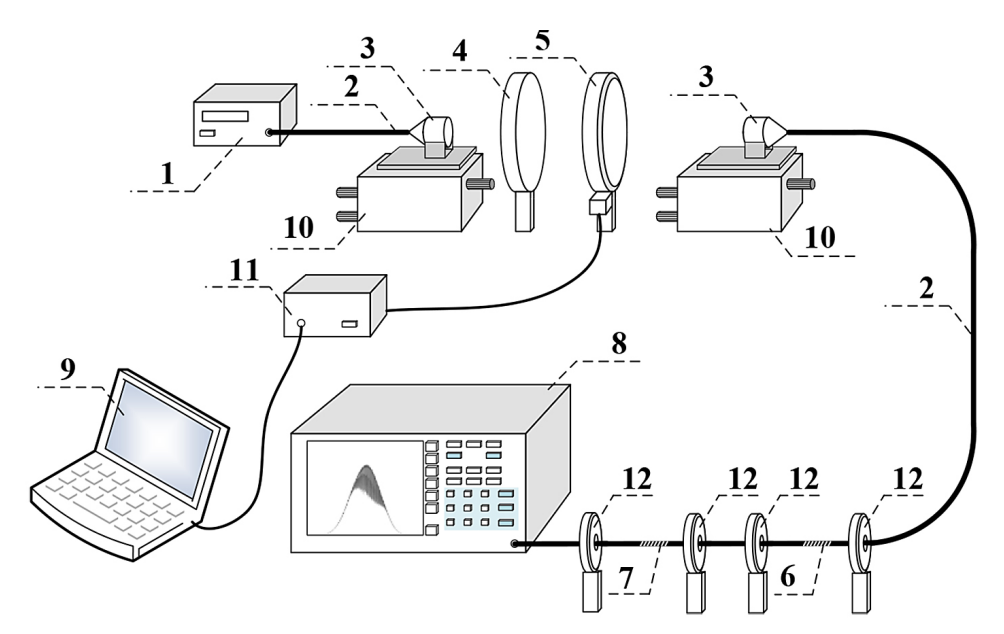


Figure 3. Interrogation setup: 1 – light source (SLED), 2 – single-mode optical fibre, 3 – collimator, 4 – polariser, 5 – half-wave plate, 6 – TFBG 1, 7 – TFBG 2, 8 – OSA, 9 – PC, 10 – 3D table, 11 – half-wave plate controller, 12 – manipulator

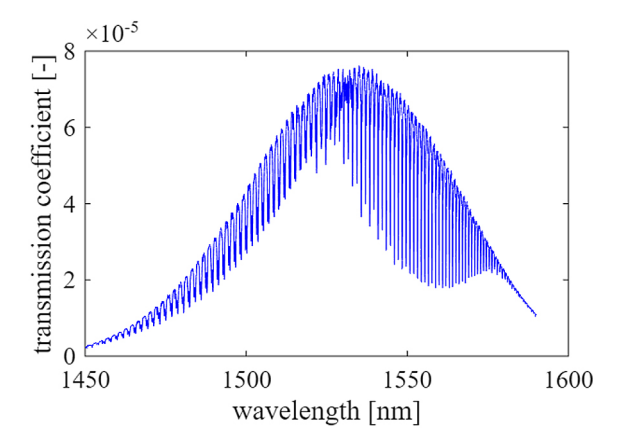


Figure 4. Spectrum of light propagating through the setup

MMC, functions

Sequence analysis is a solution that has been successfully applied in prediction and classification tasks [29, 30]. In this work, the calculation of the result was also based on sequence analysis. *MMC*₁ functions, representing the variability of the minima values of the cladding modes as a function of the LPPR angle, are created for each cladding mode's minimum by reading the minimum values at the measured rotation angles and are defined as follows:

$$MMC_{l} = \begin{cases} m_{l}(\alpha_{0}), m_{l}(\alpha_{0} + \beta), \\ ..., m_{l}(\alpha_{0} + 180^{\circ}), \end{cases}$$
(1)

where: l is the number of the successive minimum of the cladding modes, $\alpha_0 = 0^\circ$ is the initial angle of rotation of the LPPR, β is the angle of rotation by which the LPPR rotation is changed, $ml(\alpha_0 + \beta)$ is the minimum value measured for the LPPR angle equal to $\alpha_0 + \beta$. In order to obtain a continuous function, successive discrete values are connected by straight lines.

Interference assessment

Each of the obtained *MMC*₁ functions is subjected to noise assessment. The interference assessment is performed by comparing the normalised MMC₁ function with its approximation. The approximation is performed by calculating the FFT of the analysed function according to the following formula:

$$X_{k} = \sum_{m=0}^{n-1} z_{m} e^{-\frac{i2\pi km}{n}} k =$$

$$= 0, \dots, n-1$$
(2)

where: $e^{i2\pi/n}$ is a primitive n-th root of 1, z_m is the m-th sample of the processed spectrum, k is the FFT coefficient number. The processing results in a set of U coefficients:

$$X_k = \{x_0, x_1, \dots x_{U-1}\} \tag{3}$$

where: x_i is the *i*-th FFT coefficient.

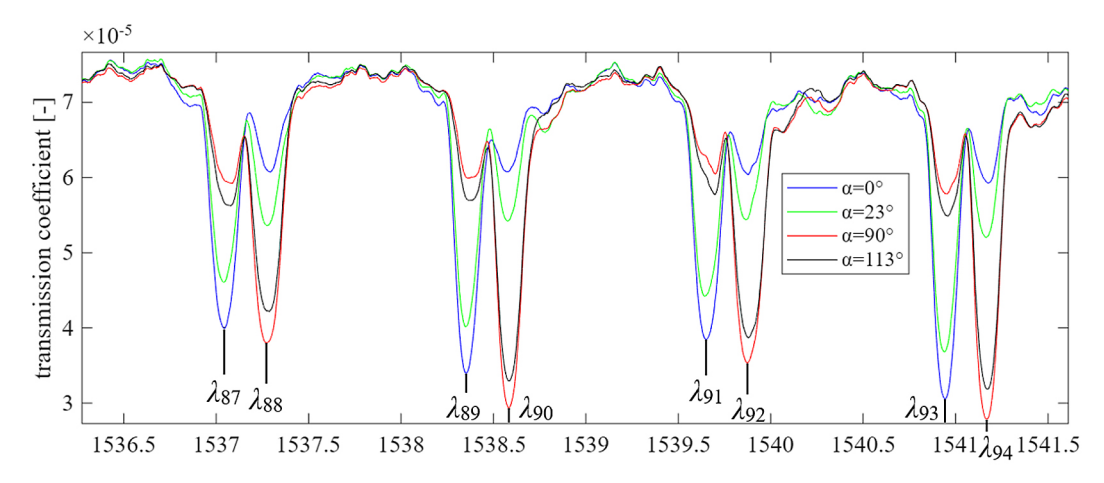


Figure 5. Minima wavelengths identification

There are eight coefficients and a constant component left in the spectrum; the rest are zeroed:

$${X'}_k = \left\{ x_0, x_1, \dots \underset{\chi_{U-8}, \chi_{U-7}, \dots, \chi_{U-1}}{\dots, \chi_{U-1}} \right\} \quad (4)$$

The inverse Fourier transform (IFFT) is calculated from the X'_k spectrum according to the formula:

$$z'_{m} = \frac{1}{n} \sum_{k=0}^{n-1} x_{k} e^{\frac{i2\pi km}{n}} n =$$

$$= 0, \dots, U - 1$$
(5)

Next, noise measures are calculated:

$$MSE = \frac{1}{M} \sum_{m=1}^{M} (z'_m - z_m)^2$$
 (6)

$$MAE = \frac{1}{M} \sum_{m=1}^{M} |z'_{m} - z_{m}| \tag{7}$$

where: M is the number of discrete values in MMC_l function, z_m is the m-th value of MMC_l function, z_m is the m-th value of MMC_l function approximation.

Calibration

Preparing the measuring system for operation requires calibration. This involves taking measurements with a specific resolution, determining the noise levels of the MMC_l functions, and permanently recording the selected functions. For this work, calibration with a resolution of 2° was employed. The half-wave plate was homed by setting it to the 0° position, after which the spectrum of light propagating through the system was measured. Next, the LPPR angle

was changed by 2° by adjusting the position of the half-wave plate, and the measurement was repeated. The change in the LPPR angle and the measurement were repeated until the angle of rotation of the light polarisation plane reached 180° . Subsequently, the obtained spectra are analysed to determine the wavelengths $A = \{\lambda_1, \lambda_2, \dots, \lambda_L\}$ at which cladding modes minima occur. Based on this, the values of spectrum samples occurring at wavelengths stored in the set A are extracted from the measurements taken for all examined LPPR angles and used to create MMC₁ functions.

Next, MMC₁ functions exhibiting significant noise were removed. To achieve this, histograms of MSE and MAE noise measures were generated. Each histogram was divided into 400 bins. In these histograms, sparse bins with high noise measures were identified. Beginning from the right side of the histogram, all bins containing fewer than five entries were marked. The marking concluded upon encountering the first bin with at least five entries. MMC₁ functions with distortion measures in the marked bins were identified and eliminated. The remaining MMC₁ functions were permanently archived for use in the LPPR angle measurement. The calibration algorithm diagram is presented in Figure 6.

Measurement

The LPPR angle is determined by measuring the spectrum (LS_m) of light propagating through the system. The LS_m spectrum provides values of samples occurring at wavelengths stored in the *minima* set. From these, the set $M = \{m_1, m_2, ..., m_p, ..., m_L\}$ is created, where m_i denotes the read value for the l-th wavelength from the set *minima*.

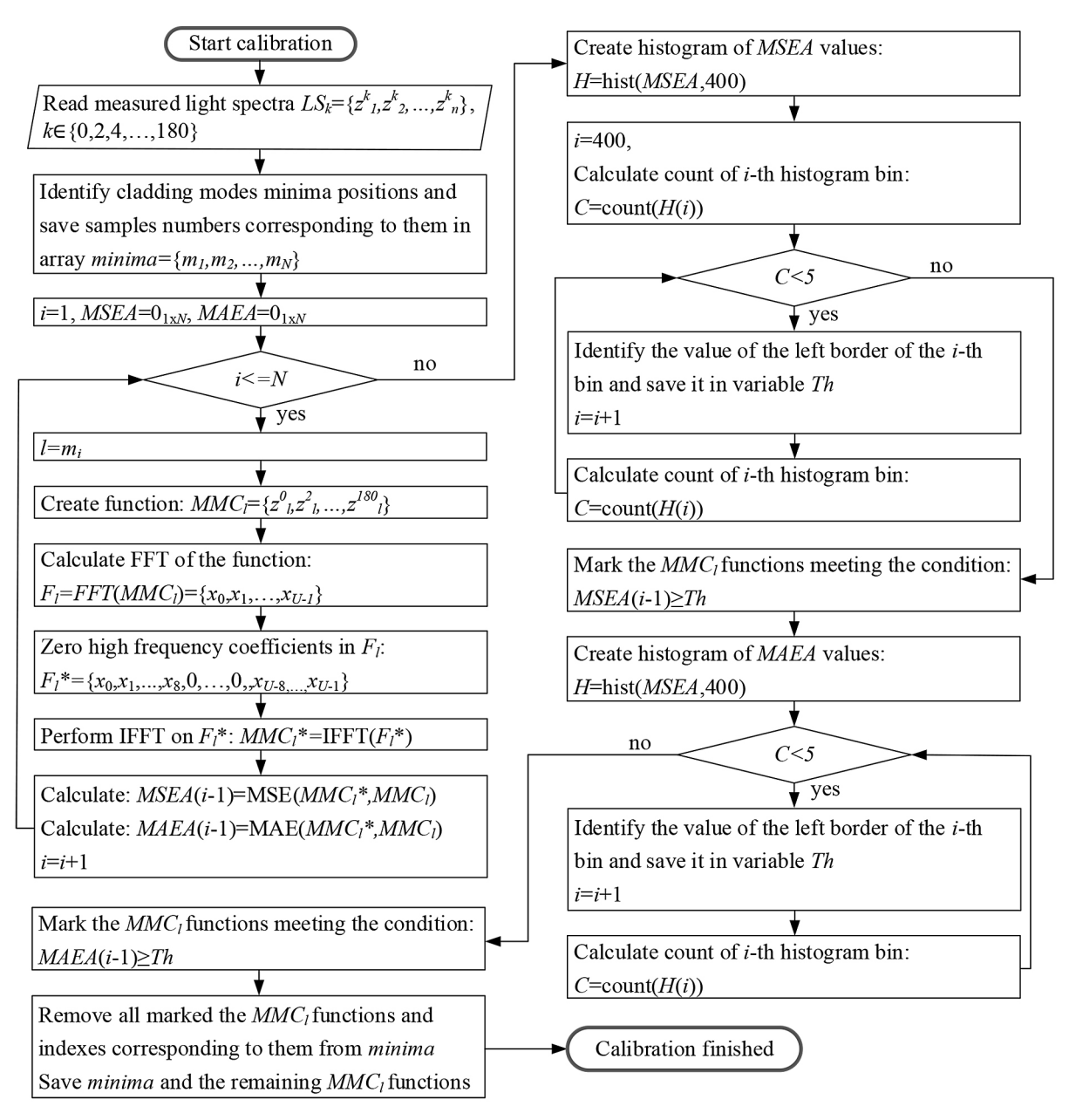


Figure 6. Calibration algorithm diagram

Next, the rotation angles are sought for which the MMC_1 functions take on the corresponding values from the set minima. This is accomplished by finding angles α for which the MMC_1 functions satisfy the condition:

$$MMC_l(\alpha) = m_l \tag{8}$$

The angles found are stored in the set α_{read} . The diagram of calculating angles to put in the α_{read} set is presented in Figure 7.

In order to estimate the value of the LPPR angle based on the results stored in the α_{read} set, a histogram analysis was used, dividing the range of values into N equal intervals (bins). Each bin

represents the frequency of occurrences of readings in a given angular range. The first step is to identify the bin with the largest number of occurrences. Its index (i) and the LPPR angles corresponding to the edges of the bin $(\alpha_{begin}$ and $\alpha_{end})$ are determined. If i=1 or i=N or if the adjacent bins are empty, then the centre of the most numerous bin is taken as the value of the rotation angle:

$$\alpha_{final} = \alpha_{begin} + w \tag{9}$$

where: w is the width of the bin calculated according to the formula:

$$w = \alpha_{end} - \alpha_{begin} \tag{10}$$

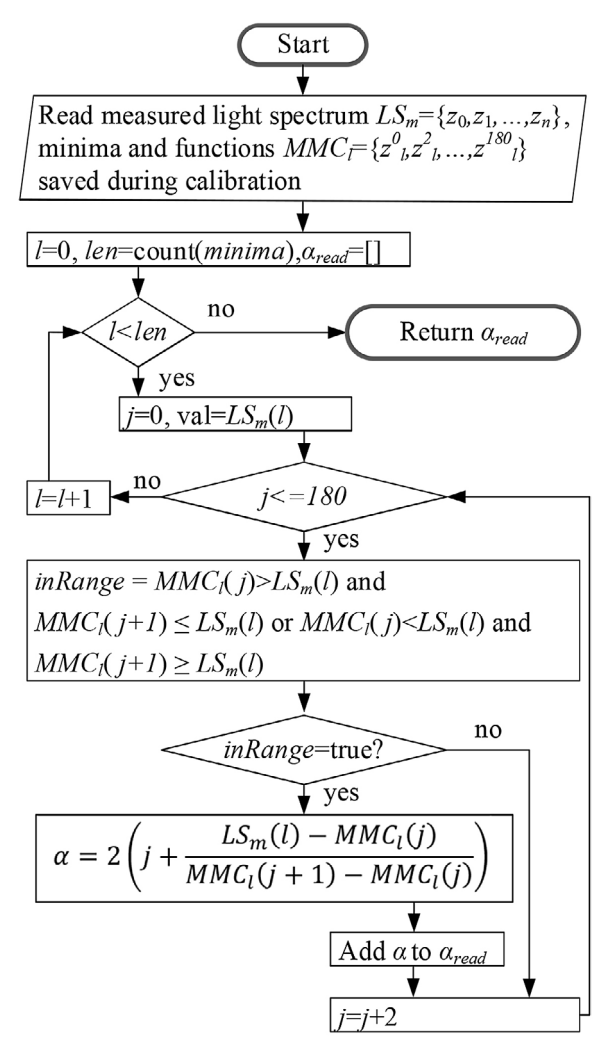


Figure 7. The algorithm to calculate rotation angles with *MCC*, functions

Otherwise, the bins adjacent to the most numerous bin are taken into account in the calculation of the final result. The angle value is estimated assuming that a continuous function can approximate the local distribution and that the maximum is closer to the adjacent bin that has a larger number of elements. The final result is calculated according to the following formula:

$$\alpha_{final} = \begin{cases} \alpha_{begin} + w + \frac{b}{c} \times w \text{ if } a = 0\\ \alpha_{begin} + \frac{b}{a+b} * w \text{ if } b \neq 0 \land a \neq 0 \\ \alpha_{begin} + w + \frac{a}{c} \times w \text{ if } b = 0 \end{cases}$$

where: a is the number of elements in bin i-1, b is the number of elements in bin i+1, and c is the number of elements in the most numerous bin i.

The approach employed enables the local distribution of data around the histogram maximum to be considered, thereby enhancing the accuracy of the estimation through interpolation based on neighbouring values. The advantage of this method lies in its computational simplicity and greater resilience to noise in the data, particularly in the context of multimodal or slightly shifted measurement distributions.

RESULTS AND DISCUSSION

Features usefullness

When measuring the LPPR angle, only those characteristics that vary in response to changes in the LPPR angle are useful. Additionally, these changes must demonstrate significant variability and low noise levels. The usefulness of features such as the minima values of cladding modes, their positions, and the FFT coefficients has been confirmed. Figure 8 shows graphs of the normalised values of the cladding modes' minima as a function of the LPPR angle. These graphs form four distinct groups of waveforms with similar shapes. Two pairs of groups display extrema at comparable LPPR angles, which are roughly mirror images of each other with respect to the line y=0.5. Each waveform pair originates from one of the TFBGs used. The analysis revealed that waveforms from a single TFBG tend to have extrema at similar LPPR angles. This results in reduced measurement accuracy within certain ranges of the LPPR angle, as reported in [19,20]. Since the measurement relies on identifying the LPPR angle at which the waveforms attain the measured value, achieving reliable results requires waveforms with a steep slope and minimal noise. This was addressed by employing a second TFBG rotated by 23 degrees relative to the first. The waveforms from TFBG 2 display a significant slope at the LPPR angles where TFBG 1's waveforms show extrema. Using two TFBGs makes it possible to identify a broad set of functions meeting these criteria for each rotation angle.

An analysis of the suitability of FFT coefficients, calculated from a spectrum fragment, for use in the calculations in question showed that they exhibit variability as a function of the LPPR angle (hereinafter referred to as the FCC_k function), but most are excessively noisy. Only coefficients with lower initial numbers can exhibit

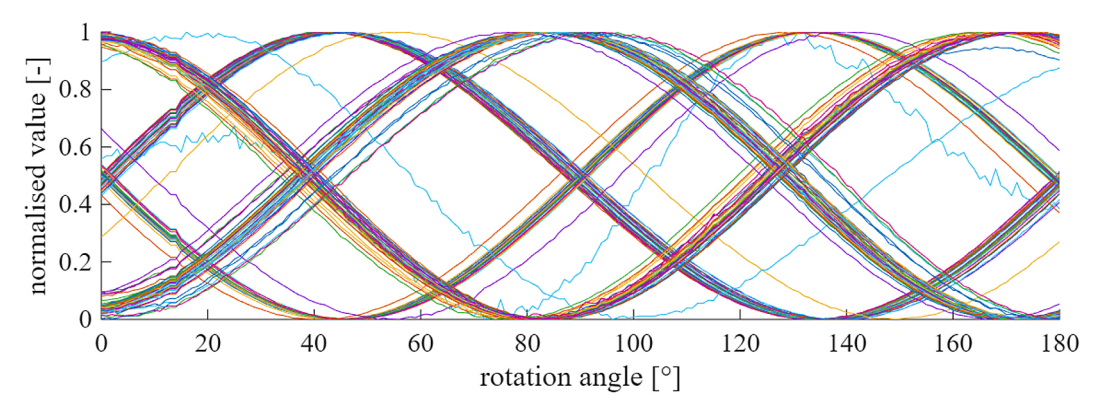


Figure 8. Cladding modes' minima values as a function of the LPPR angle

low noise levels; hence, the number of analysed coefficients was limited to the first two hundred. Furthermore, as shown in Figure 9, the gradient and noise of the FCC_k function may vary for different LPPR angles.

The verification of shifts in the minima of the cladding modes' positions showed that they indeed move with changes in the LPPR angle. However, the character of these shifts significantly restricts their usefulness in the current calculations. Figure 10 displays the changes in position of four selected minima, which show an apparent step change. This change helps clearly identify the angle range defined by the low or high value of the minimum shift. To identify which features are most helpful for the calculations, a study was conducted using random forest (RF), multilayer perceptron (MLP), and k-Nearest neighbours (KNN) algorithms to estimate the LPPR angle from different data sets. These data sets,

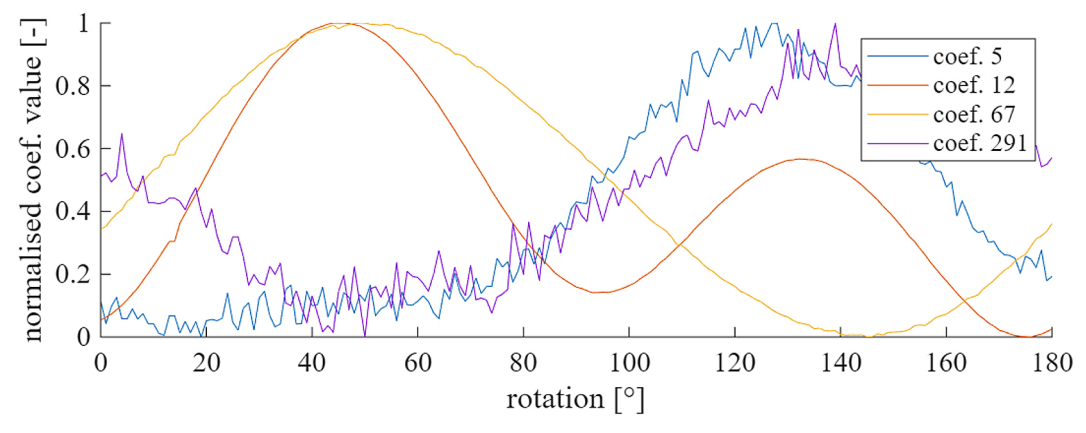


Figure 9. Normalised FCC_k functions

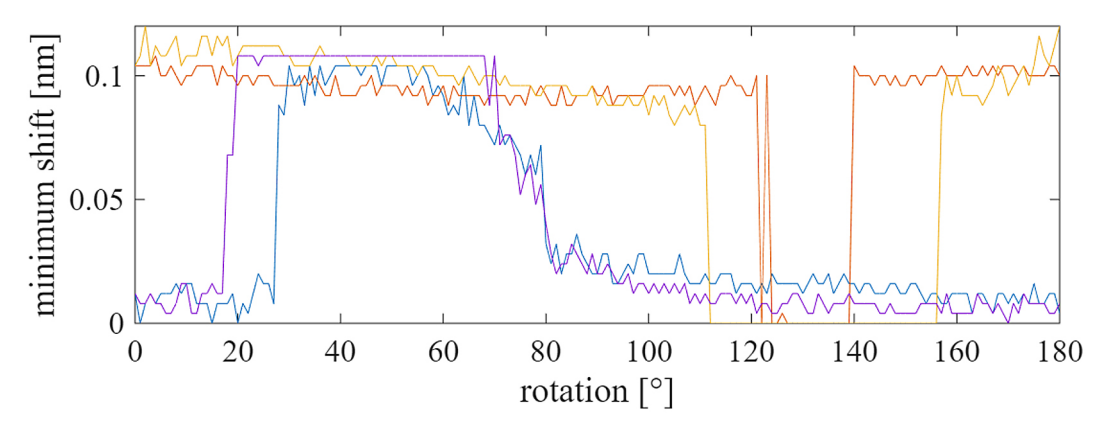


Figure 10. Chosen minima position change

obtained for LPPR angles $\alpha=0^{\circ}$, 2° , 4° ,..., 180° , were used for training. Afterwards, RF, MLP, and KNN were used to calculate the results for $\alpha=0^{\circ}$, 1° , 2° ,..., 180° , performed ten times each. The average measurement errors are shown in Table 1.

The analysis of the results showed that the smallest errors were achieved by using only the minimum values of the cladding modes in the MLP algorithm. However, for the KNN algorithm, the best results came from employing minima shifts. This indicates that both data sets can be useful in calculating the LPPR angle.

An analysis of all minima shifts showed that, for each analysed minimum, there are two significant changes in its position. However, these shifts are not evenly spread out. There are ranges of about 10° where none of the minima have shifted significantly. Analysing the position of minima outside these significant change ranges is not useful because of high noise levels and low variability. Therefore, this feature can help roughly identify the range where the calculated rotation angle lies, but it is not suitable for precise measurement, as shown by the results in Table 1. Much better results are achieved by examining changes in the minima heights; in cases with multiple minima,

these changes exhibit low noise. Using both features together (minima heights and shifts) and feeding them into one of the analysed algorithms is ineffective, as minima shifts add little useful information while introducing significant noise. Consequently, this results in lower accuracy compared to using only minima heights.

This assessment aimed to evaluate the usefulness of the examined features in calculating LPPR, which was successfully achieved. Nevertheless, none of the algorithms used in the tests produced satisfactory outcomes. The error rate was considerably higher in each case compared to the solutions presented in [19, 20]. Because of this, the author decided not to continue developing these methods or examine training with data obtained at higher resolutions.

Both the MMC₁ and FCC_k functions show variability with changes in the LPPR angle. To assess their usefulness in calculations, their noise levels were measured by calculating the MAE for all functions, then comparing the noise levels of both types. The results are shown in the histograms in Figure 11. The comparison reveals that the noise level of the *MMC*₁ function is significantly lower. Additionally, a large proportion of these functions

Table 1. Errors in calculations

Parameter	MLP		RF		KNN	
Farameter	MAE[°]	MSE [°2]	MAE[°]	MSE [°2]	MAE[°]	MSE [°²]
All minima heights, all minima shifts	12.01	294	2.17	51	1.49	3.3
All minima heights	0.91	1.48	1.95	45	3.59	157
All minima shifts	14.24	401	4.47	191	1.49	3.3

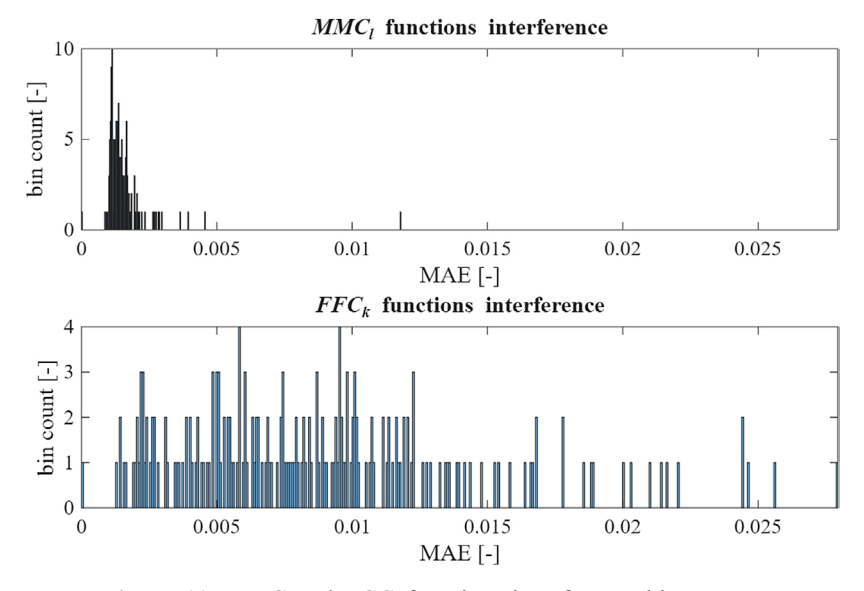


Figure 11. *MMC*₁ and *FCC*₂ functions interference histograms

have a low noise level. In contrast, the FCC_k functions display notable differences in noise levels among individual functions. Only a few have a noise level similar to most MMC_l functions. Therefore, FCC_k functions were not used in this study.

Noisy MMC, functions removal

The use of noisy MMC_l functions negatively impacts measurement precision; those exhibiting higher noise levels than most MMC_l functions have been removed. Since only few MMC_l functions show increased noise levels, they can be identified by examining which are located in the sparse bins of the MMC_l function noise histograms. Figures 12 and 13 demonstrate MMC_l function noise histograms created using MSE and MAE measures. Sparse bins are marked in red. Figure 14 shows the set of remaining functions after filtering. A comparison with the full set of functions (Figure 8) indicates that MMC_l functions with higher noise levels have been eliminated.

Measurement results

The developed method was verified by conducting measurements for rotation angles $\alpha = \{0^{\circ}, 1^{\circ}, 2^{\circ}, ..., 180^{\circ}\}$. A histogram with a bin count of 360 was used in the LPPR calculation algorithm. The re3sulting measurement data is shown in Figure 15, while the measurement errors are displayed in Figure 16.

The measurement results demonstrated that the method operates reliably across the entire measurement range, with no intervals showing increased error levels. The measurement error does not exceed 0.25°, and the MAE is 0.074°.

Additionally, the effect of the number of histogram bins on the method's performance was analysed. Figure 17 illustrates the MAE, MSE, and maximum measurement errors, which represent the largest estimation errors of the rotation angle encountered during measurements for rotation angles $\alpha = \{0^{\circ}, 1^{\circ}, 2^{\circ}, ..., 180^{\circ}\}$. Analysis of the results indicated that increasing the number of bins decreases the MAE and MSE error values.

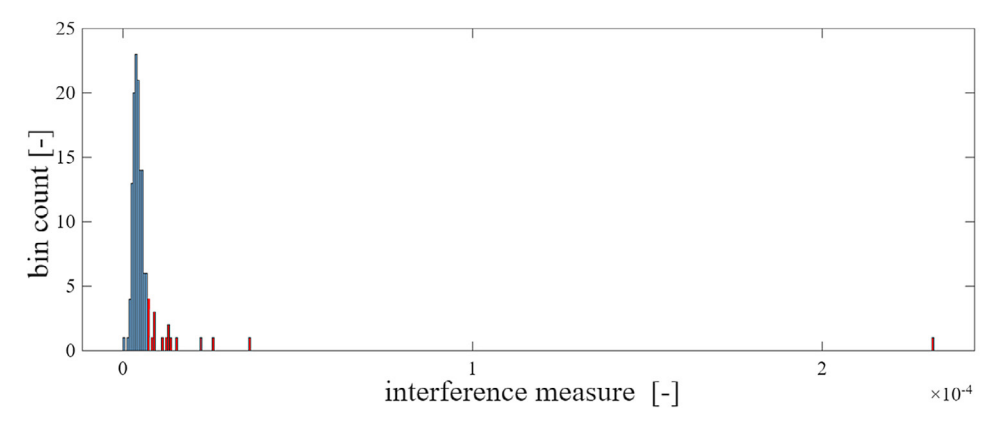


Figure 12. MMC, functions interference histogram according to the MSE measure

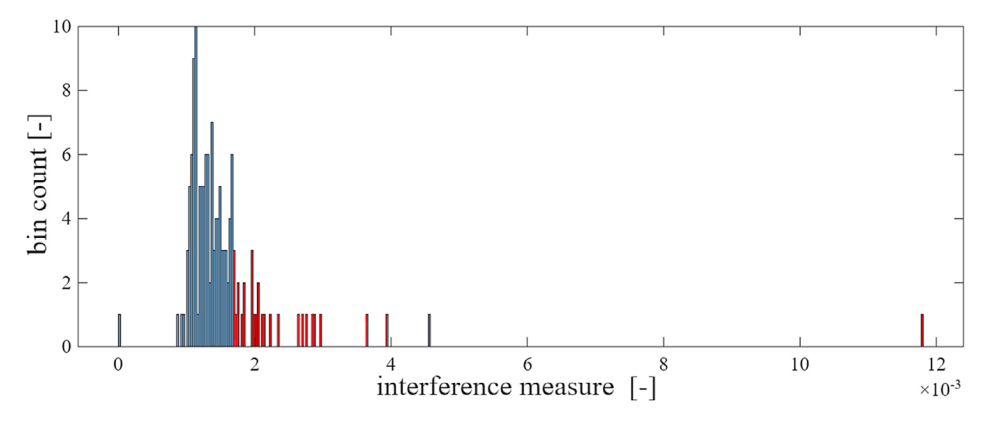


Figure 13. *MMC*₁ functions interference histogram according to the *MAE* measure

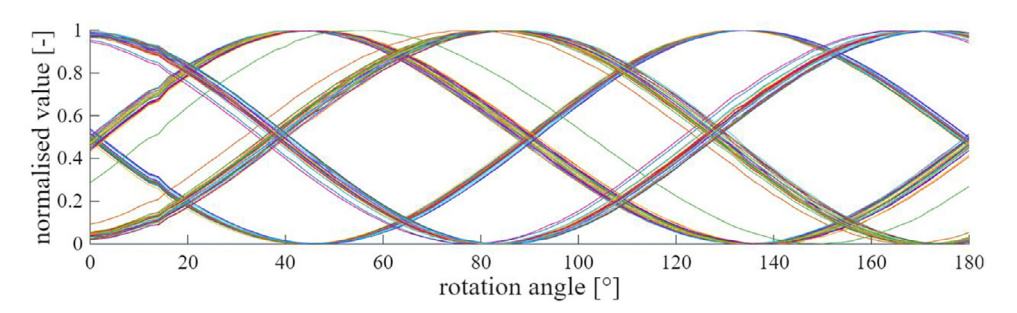


Figure 14. MMC, functions after the removal of noisy functions

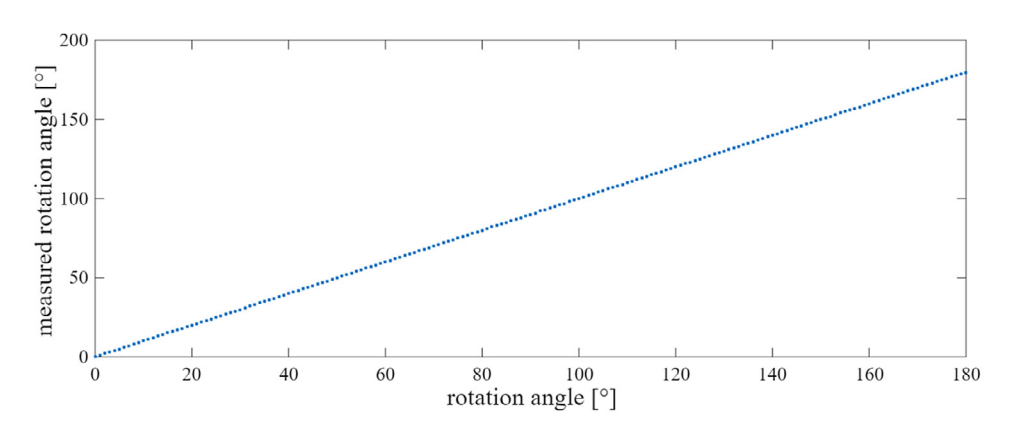


Figure 15. Measurement results

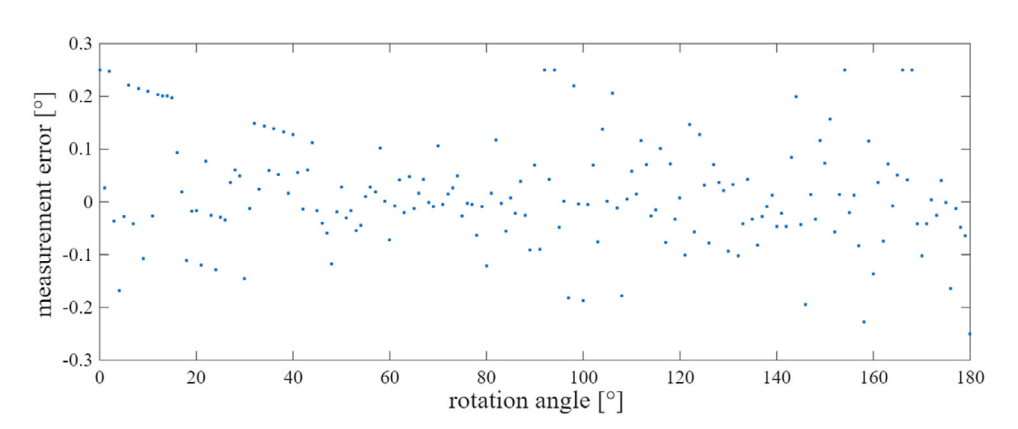


Figure 16. Measurement errors

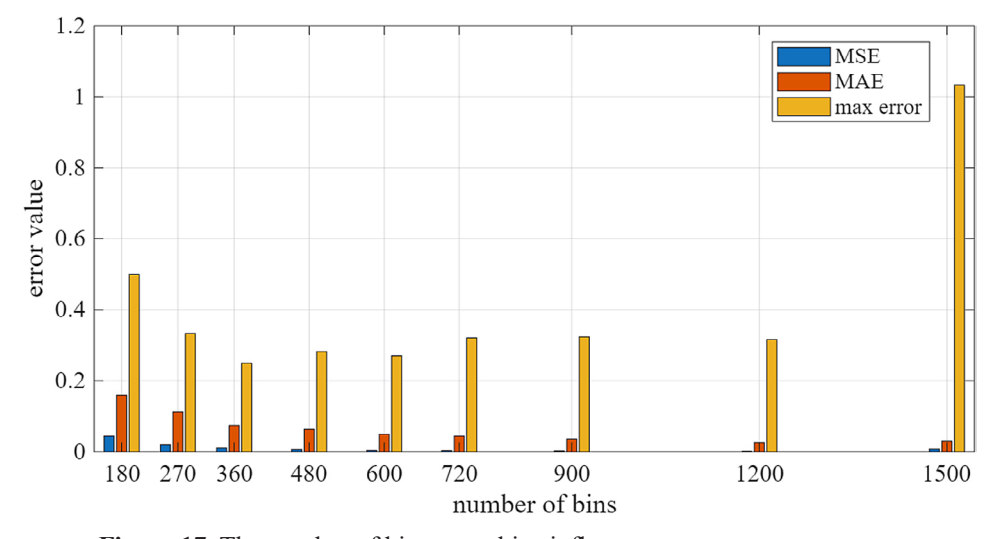


Figure 17. The number of histogram bins influence on measurement errors

This is due to the improved resolution of the histogram, which enhances the accuracy of the final calculation. However, when divided into 1500 bins or more, the MAE and MSE errors increase. The reason for this is that the number of histogram bins becomes excessively large, resulting in lower counts per bin. Consequently, the most populated bin might correspond to a different rotation angle than the actual measurement. The MAE and MSE reach their lowest values with more than 1000 bins. 360 bins were found to be the most suitable choice because the maximum measurement error was lowest at 0.25°.

In order to verify the stability of the method, measurements for rotation angles $\alpha = \{0^{\circ}, 10^{\circ}, 20^{\circ}, ..., 180^{\circ}\}$ were repeated for 3 consecutive days. The average deviation of the measurement value $MAD = 0.012^{\circ}$. This shows the repeatability of the measurement result.

Calibration resolution

One of the factors affecting the magnitude of measurement errors is the calibration resolution. Increasing it has a positive effect on measurement precision due to denser sampling of MMC_l functions. However, it is essential to note that each system must be calibrated before use. Excessive calibration resolution will therefore hurt the time and cost of system commissioning. To verify the impact of calibration resolution on measurement error, the method was verified by evaluating the MAE for a series of measurements taken for angles $\alpha = \{0^{\circ}, 1^{\circ}, 2^{\circ}, ..., 180^{\circ}\}$ performed using

a system calibrated with different resolutions. The results obtained are presented in Table 2. A reduction in the number of samples measured during calibration causes an increase in MAE. With measurements taken every 6° or more, we observe a higher rise in MAE due to the system's infrequent calibration.

Other methods comparison

To assess the method, a comparison was made with other solutions dedicated to measuring the LPPR angle. Two of the top-performing methods available in the literature were selected. A comparison of the measurement errors of these methods with the proposed method is shown in Table 3. The method proposed in this paper achieved the best results, providing the highest precision. Besides the methods compared, those presented in [17, 18] should also be noted. Their authors also studied the issue of LPPR measurement, but their methods have significantly limited applicability due to the narrow measurement range (25–70°) within which they can achieve optimal accuracy. However, none of the papers specified the measurement accuracy, focusing only on demonstrating the relationship between transmitted light power at specific wavelengths and the LPPR angle. Paper [24] suggests using cladding mode minimum shift for measurement but does not recommend any specific measurement method. The polarisation control is also analysed in [31] but only an aspect of polarisation control with the polarisation controller is discussed.

Table 2. Effect of calibration resolution on MAE

Calibration resolution	2°	4°	6°	8°
MAE	0.074°	0.19°	0.36°	0.56°

Table 3. Features of methods for measuring the light polarisation plane rotation angle

Parameter	Method [19]	Method [20]	Proposed method
MAE	0,076°	0.24°	0.074°
Max error	0.78°	3.7°	0.25°
MSE	0.03°²	0.37°2	0.01°2

Table 4. Cost and equipment of interrogation setups used in the compared solutions

	1 1	<u> </u>			
Method	TFBG [pcs]	Manipulator [pcs]	OSA [pcs]	PC [pcs]	Total cost [EUR]
Method [19]	1	2	1	1	32140
Method [20]	1	2	1	1	32140
Proposed method	2	4	1	1	33280

Another important aspect is the cost of the proposed solution. In the system shown in Figure 3, the measurement system comprises two TFBGs, a positioning system consisting of two Thorlabs PRM1/M manipulators, an OSA, and a PC. The rest of the system is used to generate polarised light with a specific orientation. Therefore, it will not be included in the comparison. In methods [19, 20], a measuring system consisting of a single TFBG with a mounting system, an OSA, and a computer was used. The approximate prices of the individual components are: OSA - EUR 30,000, TFBG - EUR 500, manipulator - EUR 320, PC - EUR 1,000. The cost comparison in Table 4 shows that the proposed system is approximately 3.5% more expensive than competing systems. However, it should be noted that the table lists components used in laboratory tests, which may be replaced with cheaper equivalents during implementation.

CONCLUSIONS

The article proposes a new interrogation set and a method for measuring the light polarisation plane rotation angle using tilted Bragg gratings. The use of a series connection of two TFBG gratings, rotated relative to each other, has enabled the acquisition of new properties of the spectrum propagating through an optical fibre. The functions of the changes in the values of individual minima are significantly shifted relative to one another in the LPPR angle function, thereby allowing the measurement result to be calculated directly based on the analysis of variations in the values of individual cladding modes minima. This also simplifies the calculations necessary to obtain the result. It is worth emphasising that the proposed method allows LPPR to be measured within the range of 0° to 180°, with a consistent measurement error not exceeding 0.25° and MAE = 0.074° .

The methods used to assess signal noise enabled the effective removal of noisy functions, retaining only those that guarantee a precise calculation result. Thanks to the use of AI algorithms such as MLP, random forest, and KNN, the significance of signal features for the calculations was identified. The main contribution and novelty of this study are:

• The implementation of two TFBGs connected in series and rotated relative to each other in the measurement system, which allows new useful spectrum features to be obtained.

- The use of the light power values of multiple cladding modes minima to calculate the rotation angle.
- An innovative method for calculating the angle of rotation of the light polarisation plane based on the measured light spectrum, allowing calculations to be executed directly on the values of the measured spectrum samples without requiring additional transformations.
- The proposed method for assessing the noise present in the waveforms utilised.
- A technique for determining the rotation angle based on a histogram containing the values of the rotation angles derived from the light power of selected coat mode minima.

REFERENCES

- Rovera A, Tancau A, Boetti N, Dalla Vedova MDL, Maggiore P, Janner D. Fiber optic sensors for harsh and high radiation environments in aerospace applications. Sens 2023;23. https://doi.org/10.3390/s23052512
- 2. Kisała P. Physical foundations determining spectral characteristics measured in Bragg gratings subjected to bending. Metrol and Meas Syst 2022;29:573–84. https://doi.org/10.24425/mms.2022.142275
- Marzejon M, Karpienko K, Mazikowski A, Jędrzejewska-Szczerska M. Fibre-optic sensor for simultaneous measurement of thickness and refractive index of liquid layers. Metrol and Meas Syst 2019;26:561– 8. https://doi.org/10.24425/mms.2019.129584
- 4. Chen Y-T, Zhou P, Chen L-Y, Gu G-Q, Wang Y-Q, Dai L-Y. Crack detection of high-strength wind turbine bolts based on fiber bragg grating sensors. Metrol and Meas Syst 2024;31:511–28. https://doi.org/10.24425/mms.2024.150283
- 5. Guo T, Liu F, Guan B-O, Albert J. Tilted fiber grating mechanical and biochemical sensors. Opt Laser Technol 2016;78:19 33. https://doi.org/10.1016/j.optlastec.2015.10.007
- Skorupski K, Miluski P, Harasim D, Klimek J, Panas P, Kisała P. Effect of Tm3+ ion doping on the possibility of Bragg resonator inscription using an excimer laser. Metrol and Meas Syst 2024;31:595–608. https://doi.org/10.24425/mms.2024.150284
- Wojcik J, Mergo P, Makara M, Poturaj K, Czyzewska L, Klimek J, et al. Technology of suspended core microstructured optical fibers for evanesced wave and plasmon resonance optical fiber sensors. In: Kalli K, Urbanczyk W, editors. PCF. II, 2008;6990,. https://doi.org/10.1117/12.783327
- Albert J, Shao LY, Caucheteur C. Tilted fiber Bragg grating sensors. Laser Photonics Rev 2013;7:83– 108. https://doi.org/10.1002/LPOR.201100039

- Liu Y, Li Y, Xu P, Yu C. Temperature and lateral pressure sensing using a sagnac sensor based on cascaded tilted grating and polarization-maintaining Fibers. Sens 2024;24. https://doi.org/10.3390/s24216779
- 10. Klimek J. The impact of changes in the apodization profile of the Bragg grating on its spectral characteristics. Przegl El 2023;99:330–3. https://doi.org/10.15199/48.2023.01.68
- 11. Ren Z, Huang Z, Wang F, Wu J, Zhou J, Wang Z, et al. Tilted fiber Bragg grating surface plasmon resonance based optical fiber cadmium ion trace detection. Sens Actuators B: Chem 2023;393. https://doi.org/10.1016/j.snb.2023.134247
- 12. Huang F, Moreno Y, Cai J, Cai L, Cai H, Dai Y, et al. Refractive index sensitivity characterization of tilted fiber Bragg grating based surface plasmon resonance sensor. J Lightwave Technol 2023;41:5737–43.
- 13. An G, Liu L, Hu P, Jia P, Zhu F, Zhang Y, et al. Probe type TFBG-excited SPR fiber sensor for simultaneous measurement of multiple ocean parameters assisted by CFBG. Opt Express 2023;31:4229–37. https://doi.org/10.1364/OE.481948
- 14. Avellar L, Marques CAF, Caucheteur C, Frizera A, Leal-Junior A. Comprehensive evaluation of tilted fiber Bragg grating (TFBG) sensors for characterizing oilwater emulsions: A study on the impact of surfactant concentration and mixing speed. IEEE Sens J 2024;24:7824–31. https://doi.org/10.1109/ JSEN.2024.3354947
- Harasim D, Cięszczyk S. A novel method of elimination of light polarization cross sensitivity on tilted fiber Bragg grating bending sensor. Metrol and Meas Syst 2022;29:737–49. https://doi.org/10.24425/mms.2022.143066
- 16. Harasim D, Kisała P, Yeraliyeva B, Mroczka J. Design and manufacturing optoelectronic sensors for the measurement of refractive index changes under unknown polarization state. Sens 2021;21. https://doi.org/10.3390/s21217318
- 17. Kisala P, Skorupski K, Cieszczyk S, Panas P, Klimek J. Rotation and twist measurement using tilted fibre bragg gratings. Metrol and Meas Syst 2018;25:429–40. https://doi.org/10.24425/123893
- Harasim D, Kusambayeva N. The optical measurement method for structural twist monitoring with using tilted Bragg grating sensor. Przegl El 2018;94:62–5. https://doi.org/10.15199/48.2018.07.15
- 19. Koziel G, Harasim D, Dziuba-Koziel M, Kisala P. Fourier transform usage to analyse data of polarisation plane rotation measurement with a TFBG sensor. Metrol and Meas Syst 2024;31:369–81. https://doi.org/10.24425/mms.2024.149698
- 20. Dziuba-Kozieł M, Kozieł G, Harasim D, Kisała P, Kochanowicz M. Method of automatic calibration and measurement of the light polarisation plane rotation with tilted Fibre Bragg grating and discrete wavelet

- transform usage. Adv Scie Tech Res J 2025;19:165–77. https://doi.org/10.12913/22998624/194890
- 21. Powroznik P, Czerwinski D. Spectral methods in polish emotional speech recognition. Adv Scie Tech Res J 2016;10:73–81. https://doi. org/10.12913/22998624/65138
- 22. Szmajda M, Chylinski M, Sacha J, Mroczka J. Three methods for determining the respiratory waves from ECG (Part II). Metrol and Meas Syst 2024;31:51–71. https://doi.org/10.24425/mms.2024.148544
- Lukaszuk T, Krawczuk J, Zyla K, Kesik J. Stability of feature selection in multi-omics data analysis. Appl Sci (Basel) 2024;14. https://doi.org/10.3390/ app142311103
- 24. Kisała P. Światłowodowe struktury periodyczne o pochylonej modulacji współczynnika załamania: właściwości i zastosowania. Lublin: Wydawnictwo Politechniki Lubelskiej; 2019.
- Sahota JK, Gupta N, Dhawan D. Fiber Bragg grating sensors for monitoring of physical parameters: a comprehensive review. Opt Eng 2020;59. https://doi.org/10.1117/1.OE.59.6.060901
- 26. Wen H-Y, Hsu Y-C, Chen S-Y, Chiang C-C. The manufacturing process and spectral features of tilted fiber Bragg gratings. Opt Laser Technol 2021;134:106615. https://doi.org/10.1016/j.optlastec.2020.106615
- 27. Singh N, Jain SC, Aggarwal AK, Bajpai RP. Fibre Bragg grating writing using phase mask technology. J Sci Ind Res 2005:64:108–15.
- 28. Jedrzejewski K, Lewandowski L, Helsztynski J, Jasiewicz W. Bragg gratings in optical fibers made by the phase mask method. In: Wojcik J, Wojcik W, editors. LGTA II., 2004;5576:45–9. https://doi.org/10.1117/12.581516
- 29. Korga S, Żyła K, Józwik J, Pytka J, Cybul K. Predictive tools as part of decission aiding processes at the airport the case of Facebook prophet library. Appl Comput Sci 2023;19:51–67. https://doi.org/10.35784/acs-2023-35
- 30. Skublewska-Paszkowska M, Powroznik P, Lukasik E. Attention Temporal Graph Convolutional Network for Tennis Groundstrokes Phases Classification. 2022 IEEE International Conference on Fuzzy Systems (FUZZ-IEEE), 2022. https://doi.org/10.1109/FUZZ-IEEE55066.2022.9882822
- 31. Shen C, Xiong L, Bialiayeu A, Zhang Y, Albert J. Polarization-resolved near- and far-field radiation from near-infrared tilted Fiber Bragg gratings. J Lightwave Technol 2014;32:2157–62. https://doi.org/10.1109/JLT.2014.2319831
- 32. Qin H, Shen Q, Ou J, Zhu W. Long-term monitoring reliability and life prediction of fiber Bragg grating-based self-sensing steel strands. Advances in Civil Engineering 2020;2020:1–12. https://doi.org/10.1155/2020/7687039